

Alpha particle production from novel targets via laser-driven proton-boron fusion

D. P. Molloy ^{1,2,*} D. Orecchia ³ M. Tosca ^{4,5} A. Milani ³ M. Valt ⁶ A. McNamee ¹ C. R. J. Fitzpatrick ¹
 V. Kantarelou ⁴ J. P. Kennedy ¹ P. Martin ¹ G. Nersisyan ¹ K. Biliak ⁵ M. Protsak ⁵ D. Nikitin ⁵ M. Borghesi ¹
 A. Choukurov ⁵ L. Giuffrida ^{4,7} S. Kar ¹ A. Maffini ³ M. Passoni ³ A. Picciotto ⁶ and D. Margarone ^{1,4,7}

¹Centre for Light-Matter Interactions, School of Maths and Physics, [Queen's University, Belfast](https://www.qub.ac.uk), Belfast BT7 1NN, United Kingdom

²HB11 Energy Holdings Pty, Freshwater 2096, Australia

³Department of Energy, [Politecnico di Milano](https://www.politecnico.mi.it), Milan 20156, Italy

⁴[ELI Beamlines Facility](https://www.eli-beamlines.eu), The Extreme Light Infrastructure ERIC, Dolní Brežany 252 41, Czech Republic

⁵Department of Macromolecular Physics, Faculty of Mathematics and Physics, [Charles University](https://www.cuni.cz), Prague 180 00, Czech Republic

⁶Sensors and Devices Centre, [Bruno Kessler Foundation](https://www.bruno-kessler.it), Trento 38123, Italy

⁷[Laboratori Nazionali del Sud](https://www.laboratori-nazionali.it), Istituto Nazionale di Fisica Nucleare, Catania 95123, Italy



(Received 19 September 2024; accepted 2 December 2024; published 28 February 2025)

Novel targets were implemented in the beam-driven (in-target) proton-boron fusion with beneficial characteristics (chemical composition and density) compared to the commonly used boron nitride. A fusion-generated alpha particle flux of up to $(5 \times 10^7 \text{ sr}^{-1} \text{ J}^{-1})$ was generated via the proton-boron fusion reactions when irradiating the targets with a moderate laser system (10 J, 800 fs, $10^{19} \text{ W cm}^{-2}$). Normalized by laser energy, the alpha particle flux generated in this experiment is comparable with the highest alpha particle yields reported in the literature. We present experimental results with supporting simulations and calculations of the expected alpha particle yield.

DOI: [10.1103/PhysRevResearch.7.013230](https://doi.org/10.1103/PhysRevResearch.7.013230)

I. INTRODUCTION

Over the past two decades, there has been a growing interest [1–4] on the proton-boron11 $p^{11}\text{B}$ fusion reaction ($p + {}^{11}\text{B} \rightarrow 3 \cdot \alpha + 8.7 \text{ MeV}$) [5]. The $p^{11}\text{B}$ fusion reaction is aneutronic [5] and coupled with the abundant availability of ${}^{11}\text{B}$ fuel, representing 80% of naturally occurring boron [6] makes the reaction a popular and possible alternative to deuterium-tritium fusion for energy generation. Beyond energy production, $p^{11}\text{B}$ fusion could be used as a secondary source of energetic alpha particles [7], offering promising medical applications such as the production of radioisotopes for use in medical imaging [8] or to enhance the effectiveness of proton therapy [9,10].

The $p^{11}\text{B}$ fusion reaction cross section has two peaks at 150 keV and 612 keV in the center-of-mass frame, corresponding to a cross section of 0.1 b and 1.4 b, respectively [11–13]. Using high-intensity lasers ($I\lambda_{\text{um}}^2 > 10^{18} \text{ W cm}^{-2} \mu\text{m}^2$ where I is laser intensity and λ_{um} is the laser wavelength in μm) it is possible to accelerate protons and heavier ions via target-normal sheath acceleration (TNSA) [14] or hole-boring radiation-pressure acceleration (HB-RPA) [15,16] to the several MeV energies, which are

sufficient to drive $p^{11}\text{B}$ fusion reactions efficiently. It has also been demonstrated experimentally that it is possible to initiate $p^{11}\text{B}$ fusion reactions driven by protons in the 100s of keV range, even while using relatively modest laser intensities ($\approx 10^{16} \text{ W cm}^{-2}$) [17,18].

Two target geometries are regularly used in laser-driven $p^{11}\text{B}$ experiments: (1) pitcher-catcher, where one target supplies the energetic fuel ion beam, which irradiates a secondary catcher target generating the alpha particles [7,19,20], (2) in-target, where a target rich in both hydrogen and boron-11 is directly irradiated by the laser [17,18,21–24]. Natural boron or boron-nitride (BN) targets have been frequently used in the in-target configuration [17,21,24]. However, the hydrogen content here is estimated to be only a few % and is present owing to contamination during manufacturing and hydrocarbon surface contamination [17,25].

This study explores the effectiveness of new targets for alpha particle generation through $p^{11}\text{B}$ fusion. All targets have the advantage of a significantly higher hydrogen content compared to B and BN targets used in previous experiments. Three types of target compositions were examined: low-density ($\approx 100 \text{ mg cm}^{-3}$) hydrocarbon layers on a thick BN target, low-density ($\approx 100 \text{ mg cm}^{-3}$) boron and hydrocarbon foams, and solid-density (0.9 g cm^{-3}) ammonia-borane (NH_3BH_3). Using these novel targets and a 10 TW laser system, it was possible to generate over $5 \times 10^8 \alpha/\text{sr}$, i.e., $5 \times 10^7 \alpha/\text{J}/\text{sr}$, which is comparable with the highest yields per joule currently reported [17,24]. Radiative-hydrodynamic and particle-in-cell (PIC) simulations were performed to model the laser-plasma interaction and assess the acceleration of the fuel ions (hydrogen and boron) for the different target configurations.

*Contact author: dmolloy09@qub.ac.uk

Published by the American Physical Society under the terms of the [Creative Commons Attribution 4.0 International license](https://creativecommons.org/licenses/by/4.0/). Further distribution of this work must maintain attribution to the author(s) and the published article's title, journal citation, and DOI.

TABLE I. Summary of targets investigated during the experimental campaign.

Deposition	Thickness (μm)	ρ (mg cm^{-3})	Substrate	Thickness (mm)	ρ (g cm^{-3})
			BN	1.5	2.1
			NH_3BH_3	3.0	0.9
B + CH_2 Foam	60	80	$(\text{C}_3\text{H}_6)_n$	1.0	1.0
CH_2 Foam	20	120	BN	1.5	2.1
ppC:H NPs	10–25	130–170	BN	1.5	2.1

II. EXPERIMENTAL SETUP

A. Laser System

The experimental campaign was performed at the Centre for Light-Matter Interactions at Queen’s University Belfast using the 10 TW TARANIS laser system [26]. The TARANIS laser, of wavelength 1053 nm, delivered between 8–10 J on target, in 800 fs. Using an $f/3$ parabola, the beam was focused to a focal spot with a full-width-half-maximum (FWHM) of 5.1 μm corresponding to an average intensity of $2 \times 10^{19} \text{ W cm}^{-2}$ across the FWHM. The 1.5 ns pedestal has a contrast ratio of 5×10^{-7} . The p-polarized laser, incident at 20° to target-normal, directly irradiated the surface of various targets containing both boron and hydrogen (in-target scheme). It has previously been demonstrated using the same laser system that it is possible to accelerate protons with energies up to 3 MeV from the front surface into target bulk and drive p^{11}B fusion reactions [27].

B. Targetry

This experimental campaign investigated the suitability of several novel targets, detailed in Table I, for use in in-target proton boron fusion experiments. A diagram of the laser and target configuration is provided in Fig. 1. During the campaign, we investigated three different target composition categories.

As discussed, the hydrogen content within the BN target is very low (a few %), and any significant laser prepulse will quickly ablate the few nanometers of water and hydrocarbon surface contaminants [25] before the arrival of the main pulse. Therefore, it is expected that the p^{11}B fusion yield would be enhanced by increasing the hydrogen content of the target. Motivated by the work presented in [27], in which plasma polymers in the form of thin films were deposited on a BN substrate to increase the hydrogen density at the surface of the target, in this campaign, low-density ($\approx 10\%$ solid-density) plasma polymerized hydrocarbon nanoparticles (ppC:H NPs) and polyethylene foams were deposited on a BN substrate. In this scheme, the low-density hydrocarbon deposition is designed to act as a hydrogen “reservoir”, ensuring that a sufficient number of protons can be accelerated into the BN target containing a high density ($5 \times 10^{22} \text{ cm}^{-3}$) of boron ions. The deposits of ppC:H NPs were prepared by plasma polymerization of hexane using a gas aggregation cluster source (GAS) similar to the procedure described in [28,29]. Two depositions with different densities and thicknesses (10 μm thick with a density of 170 mg cm^{-3} and 25 μm thick with a density of 130 mg cm^{-3}) were produced. The ppC:H NPs mean and standard deviation of the nanoparticle diameters were 550(40) nm

and 64(8) nm, respectively. A set of targets was produced via femtosecond pulsed laser deposition (fs-PLD) to obtain a 20 μm -thick, 120 mg cm^{-3} polyethylene foam deposition on top of a BN target. The nanostructure of polyethylene foam is composed of 100–500 nm diameter nanoparticles.

The second target used was 3-mm-thick, solid-density (0.9 g cm^{-3}) ammonia-borane (NH_3BH_3) disks. The production process and detailed target characterization is available in [30]. While maintaining a similar boron ion density as BN, there is, in this case, a high density of hydrogen throughout the bulk target. This is advantageous not only for facilitating a substantial flux of protons to be accelerated from the target surface into the target bulk but also because the high hydrogen density throughout the bulk (NH_3BH_3) target could be beneficial under conditions where the production of a supra-thermal proton population via elastic scattering from fusion-generated alpha particles could significantly contribute to further alpha particle production [31,32].

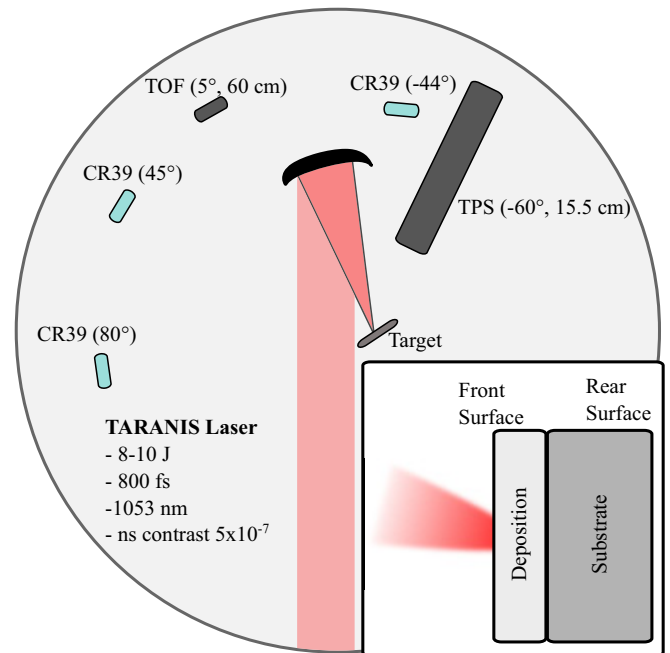


FIG. 1. Schematic of the TARANIS target chamber. Colombia Resin No. 39 (CR39) detectors are placed at three positions observing the front surface of the target. The time-of-flight (TOF) diamond detector is placed at 5° to target-normal at a distance of 60 cm and a Thomson parabola spectrometer (TPS) was placed at 60° to target-normal at a distance of 15.5 cm. The inset image shows a schematic of the targets. The characteristics of the targets are described in Table I.

TABLE II. Summary of aluminium (Al) filters used on CR39 and associated cut-off energies of alpha particles and boron ions calculated using SRIM [37].

Al thickness [μm]	α -particle cutoff [MeV]	Boron-11 cutoff [MeV]
6.5	2.0	6.2
10	2.8	9.6
14	3.7	13.2

The final target category is a low-density (80 mg cm^{-3}) boron and polyethylene foam layer deposited on a solid polypropylene substrate. Such low-density foam targets have been shown to improve the absorption of laser energy by the target [33]. A benefit of the “pure” boron foams is the absence of a significant density of other ions (i.e., nitrogen in BN and (NH_3BH_3) targets), which do not contribute to the fusion yield. The boron foams are produced via fs-PLD, which allows the foam density, nanostructure morphology, and composition to be controlled. The production process and typical characteristics of the foam depositions are described in detail in [34]. While hydrogen will be naturally present in the foam owing to hydrocarbon contamination, the targets were produced with a codeposition of boron and polyethylene to further increase the hydrogen content within the foam. Using energy-dispersive x-ray spectroscopy to measure the C and B atomic ratios, the boron-to-hydrogen ratio of the foam codeposition was estimated to be 1:1.4, under the assumption that the C:H ratio remained the same as the original polyethylene target (approximately 1:2).

C. Diagnostics

During the laser-plasma interaction, protons and heavy ions (i.e., boron, carbon, and nitrogen) are accelerated over a broad range of angles. Because of their high sensitivity to individual charged particles, Colombia Resin No. 39 (CR39) nuclear track detectors are regularly implemented to discriminate $p^{11}\text{B}$ fusion-generated alpha particles from other energetic ions [24,35]. When energetic ions irradiate the CR39, the structure of the polymer is damaged. Following etching in 6.25 M NaOH at 70°C , the damage appears as visible, dark tracks, as the damaged polymer is etched at a greater velocity than the bulk CR39 material. These particle tracks can be imaged using an optical microscope.

The size of particle tracks depends on the charge and energy of the incident particles [24,35]. In principle, it is possible to discriminate alpha particles from the proton and heavier ions tracks present on CR39 detectors. However, because of the broadband energy spectra of the other energetic ions (i.e., protons, carbon, and boron ions) generated in a laser-plasma interaction and the statistical nature of ion energy loss, the track dimensions of the various species can overlap, sometimes making it challenging to assess the alpha particle yield [24,36].

Aluminium (Al) filters of thicknesses ranging from 6.5–14 μm were placed on each CR39 detector, as summarized in Table II. The filtering has two roles: (1) shielding the CR39 from the high flux of low energy particles, preventing

saturation of the detector, and (2) providing information on the energy distribution of the alpha particles. Depending on the effectiveness of the acceleration of heavy ions, the Al filters can also block a significant flux of heavy ions, improving the confidence of alpha particle detection. Based on calibration data obtained using conventional accelerators at INFN-LNL [36,38] (see Appendix A), alpha particles with energies in the range 0.5–3.7 MeV are expected to produce tracks with areas ranging from 1 to 5 μm^2 . The majority of alpha particles generated via the 675 keV resonance have an energy of ≈ 4 MeV [39]. Therefore, after escaping the target and passing through the Al filters, the fusion-generated alpha particles should produce particle tracks with areas within our calibration range.

Because of the thickness of the target ($\approx \text{mm}$), alpha particles cannot escape the rear surface of the target. Therefore, all CR39 diagnostics were placed observing the front surface of the target. Three CR39 detectors were placed at -45° , 44° , and 80° (see Fig. 1) at distances of (50 cm, 49 cm, and 45 cm) in single shot mode or (70 cm, 67 cm, and 64 cm) when accumulating more than one shot.

A Thomson parabola spectrometer (TPS) and time-of-flight (TOF) diamond detector were used to characterize the ion flux generated in the interaction during each shot. A TPS was placed at an angle of 60° relative to the target normal, observing the front surface of the target as seen in Fig. 1 and was equipped with a 600 μm diameter entrance pinhole. The TOF detector was positioned at 5° relative to the target normal, at a distance of 60 cm, and was shielded with a 6.5 μm aluminum filter.

III. EXPERIMENTAL RESULTS

The proton energy spectrum extracted from the Thomson parabola for several targets is presented in Fig. 2(a), noting that the maximum detectable energy of the diagnostic is ≈ 2.5 MeV. Figure 2(b) shows the results for four shots measured using the TOF diamond detector. Assuming all ions are fully ionized, boron, carbon, and nitrogen ions will have a charge-to-mass ratio of ≈ 0.5 . Therefore, given the same accelerating potential, the maximum energy of these heavier ions will be $\approx 50\%$ of the proton cut-off energy. However, it is well known that because of their higher charge-to-mass ratio, protons are preferentially accelerated and will partially deplete the accelerating field. Heavier ions, therefore, typically experience a reduced accelerating potential. Considering the proton energies detected by the TOF and TPS (≈ 2 MeV), the flux of heavier ions that are energetic enough to reach the filtered regions of the CR39 nuclear track detectors is expected to be very low. In several shots, the filtering appeared sufficient to stop all heavy ions.

A 1-mm-thick polypropylene target was irradiated as a reference for the typical ion emission from thick targets. Figure 3(a) shows a portion of the raw CR39 image and the resulting distribution of particles detected by CR39 placed at 80° to target normal and shielded by a 6.5 μm Al filter. The production of $p^{11}\text{B}$ fusion alpha particles is not expected from this target owing to the absence of boron. Therefore, the particle tracks observed in Fig. 3(a) are entirely caused by protons or carbon ions. The small particle tracks (below $\approx 2 \mu\text{m}^2$) are generated by the high flux of proton ions [38].

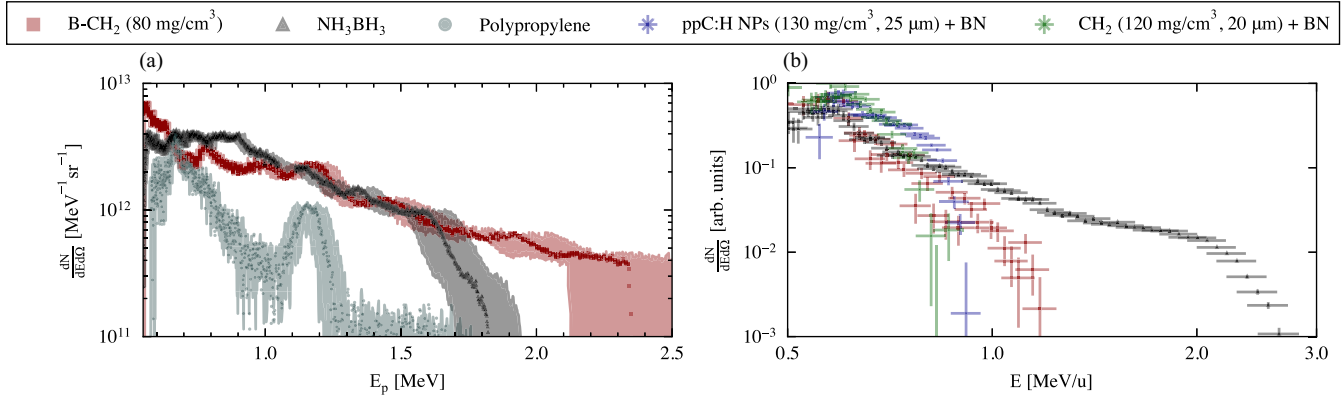


FIG. 2. Summary of the energy spectrum of backward accelerated protons detected using (a) a Thomson parabola placed at 60° to target normal at a distance of 150 mm and (b) a time-of-flight diamond detector placed at 5° to target normal, at a distance of 600 mm.

There is a negligible contribution of tracks with areas greater than $\approx 2 \mu\text{m}^2$, which would be associated with heavier ions (carbon, oxygen, etc.). This is expected as ion acceleration via the TNSA mechanism is typically less effective in very thick targets owing to the absence of hot-electron refluxing [40] and the long-scale length preplasma present at the front surface of the target, produced by the laser pedestal [41]. Below $\approx 2 \mu\text{m}^2$, the proton and alpha particle track distributions can overlap; therefore, if the proton flux is very high, the alpha particle signal in this region can be hidden.

Two components are visible in the track area distribution in Fig. 3(b) obtained from CR39, 80° to target normal following irradiation of an (NH_3BH_3) target. As in Fig. 3(a), tracks with areas less than $2 \mu\text{m}^2$ are associated with protons. The second component falls entirely within the range expected because of fusion-generated alpha particles ($1\text{--}5 \mu\text{m}^2$) based on our calibration data.

Figure 3(c) displays the track area distribution extracted from CR39 placed 45° to target normal after irradiation of the B-CH₂ foam. Three components of the track distribution can be identified. The track area of the third “peak” extends to $\approx 8 \mu\text{m}^2$, which is significantly beyond the track size expected from alpha particles when considering the calibration data and what is observed in Fig. 3(b). Therefore, the third peak must be attributed to higher-charge ions such as boron, nitrogen, and carbon, which have been efficiently accelerated in the interaction and can pass through the $6.5 \mu\text{m}$ Al filter. Note that these larger tracks were also present on the CR39 shielded by $10 \mu\text{m}$ and $14 \mu\text{m}$ thick Al as well. This apparent third peak was observed when irradiating B-CH₂ foam targets and BN targets with low-density hydrocarbon depositions. The authors suggest that this could be because of low hydrogen contamination in the case of the BN targets, which results in more energy being coupled to heavier (B, N, C) ions. The

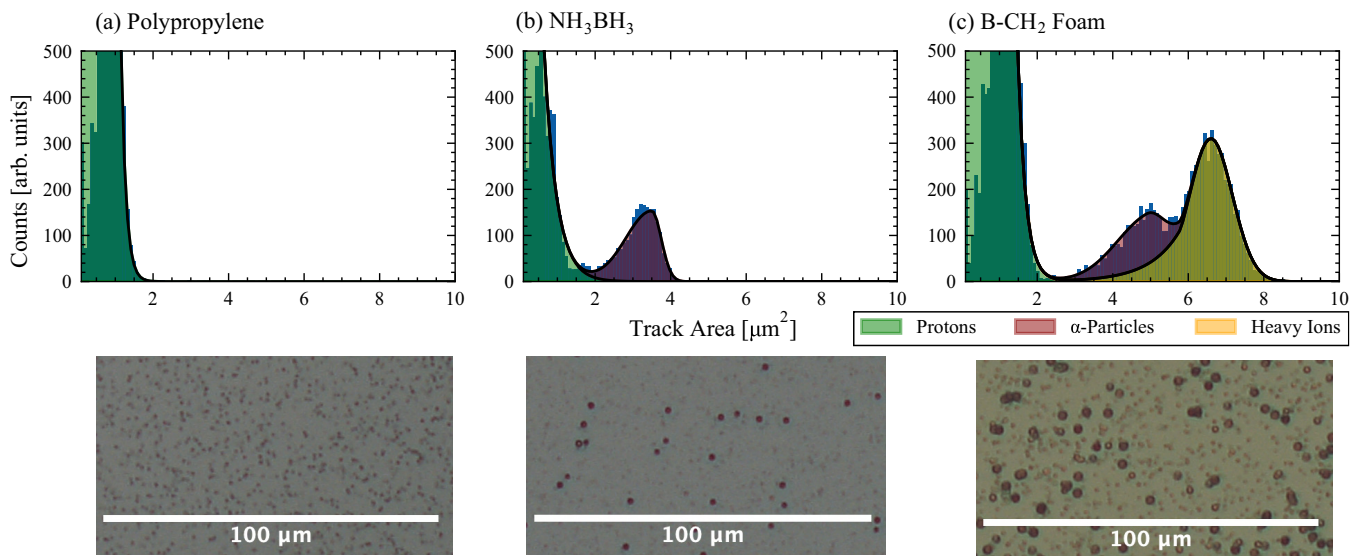


FIG. 3. Particle track area histograms and a section of the corresponding CR39 image after etching in 6.25 M NaOH for 60 min. The CR39 detectors were shielded with a $6.5 \mu\text{m}$ Al filter. (a) 1 mm Polypropylene target, CR39 placed 80° to target normal, (b) 3 mm ammonia-borane (NH_3BH_3) target, CR39 placed 80° to target normal, and (c) $100 \mu\text{m}$ B-CH₂ foam target (80 mg cm^{-3}), CR39 placed 45° to target normal. The track area histograms are separated into components expected to be associated with protons, alpha particles, and heavy ions.

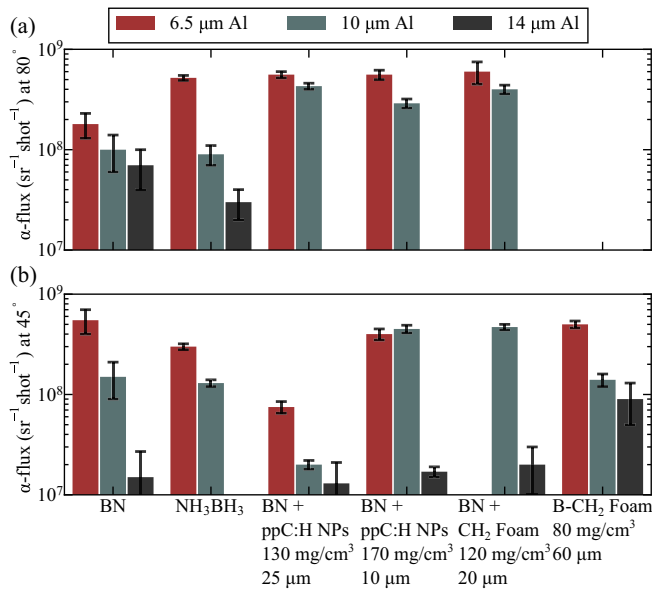


FIG. 4. α -particle yield extracted from CR39 nuclear track detectors (a) at 80° and (b) at 45° to target normal. The alpha particle yield is reported for three regions of the CR39 detector shielded by Al filters of thickness $6.5 \mu\text{m}$, $10 \mu\text{m}$, and $14 \mu\text{m}$.

low-density boron and hydrocarbon depositions can enhance laser absorption, resulting in improved ion acceleration [33].

In Fig. 3, the distributions have been fitted with empirical functions to separate the different components in the CR39 track distributions. An exponential decay (marked in green) was used to fit the proton component of the distribution. This function appears to fit the proton component of the distribution well in all cases. Heavier ions can create a broad range of track sizes depending on their energy. The heavy ion distribution was fitted with a Gaussian distribution (marked in yellow), which decays exponentially to lower pit diameters. This distribution shape was used to account for smaller particle tracks generated by energetic heavier ions. The alpha particle component was fitted using an asymmetric Gaussian distribution (marked in red). The three components were fit simultaneously using a 100 000 iterations long, Markov chain Monte Carlo using the Metropolis-Hastings algorithm. The alpha particle flux was calculated by integrating the alpha particle component of the fitting function. The mean alpha particle flux and associated uncertainty were calculated from the statistical mean and standard deviation of the integrated area. In Fig. 3(c), three peaks are observed, where the third peak is attributed, as mentioned earlier, to heavier carbon and boron ions. In Fig. 3(b), it is assumed there is no heavy ion signal owing to the absence of a secondary peak observed in Fig. 3(c).

The alpha particle flux extracted from the CR39 detectors is presented in Fig. 4. Because of the shot-to-shot variation from the laser system and the large uncertainty associated with CR39 analysis, it is not possible to identify whether, amongst the targets explored, any of them is better suited for applications in $p^{11}\text{B}$ fusion. However, each target tested here shows promising results with a maximum alpha particle flux of $5 \times 10^8 \text{ sr}^{-1}/\text{shot}$ detected in the region shielded

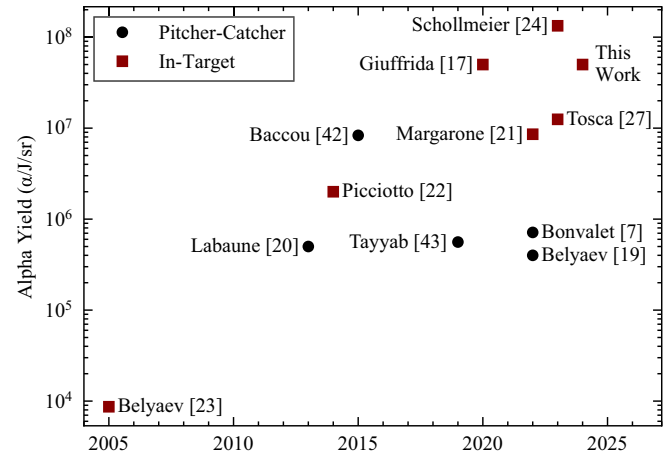


FIG. 5. Previous experimental alpha particle yields generated via laser-driven proton-boron11 $p^{11}\text{B}$ fusion reactions normalized by laser energy and separated by target geometry [7,17,19–24,27,42,43].

by a $6.5 \mu\text{m}$ filter. This represents up to a fivefold increase in alpha particle flux compared to a previous experimental campaign using the TARANIS laser system, which employed thick BN targets with a μm -scale hydrocarbon film on the surface [27]. Normalizing by laser energy, these results (up to $5 \times 10^7 \alpha/\text{sr}/\text{J}$) are comparable with the highest fluxes of alpha particles generated using kJ class laser pulses [44] and highly relativistic laser intensities [24], as shown in Fig. 5. The alpha particle yield generated from the BN with hydrocarbon deposition targets could be further increased using natural boron instead of BN as the substrate. Considering the B- CH_2 foam target, the CR39 detectors placed 45° to target normal featured a significant number of particle tracks attributed to protons, alpha particles, and heavy ions. However, while the CR39 placed at 80° to target normal had a significant proton flux, the number of larger tracks was negligible, and no significant alpha particle flux was identified. This was not observed with any other targets and is expected to be ascribable to the considerable ablation of the thick foam deposition by the pedestal, resulting in fusion occurring deeper into the target, therefore blocking the line-of-sight to the CR39 placed at 80° .

The energy distribution of alpha particles is peaked at $\approx 4 \text{ MeV}$ given an incident proton energy of 675 keV [39]. Therefore, only the alpha particles generated very near the surface of the target have enough energy to pass through the $14 \mu\text{m}$ Al filter (see Table II), resulting in the low alpha particle flux present behind this filter.

IV. MODELING AND NUMERICAL CALCULATIONS

A. Hydrodynamic Simulations

Because of the moderate contrast of the TARANIS laser system, the nanosecond pedestal causes significant preplasma generation and target ablation. The FLASH radiative-hydrodynamic code [45,46] can be used to effectively model the preplasma formation from interactions with ns pedestals and intensities low enough that collisional processes dominate the interaction [47]. The interaction of a 1.5-ns pedestal with

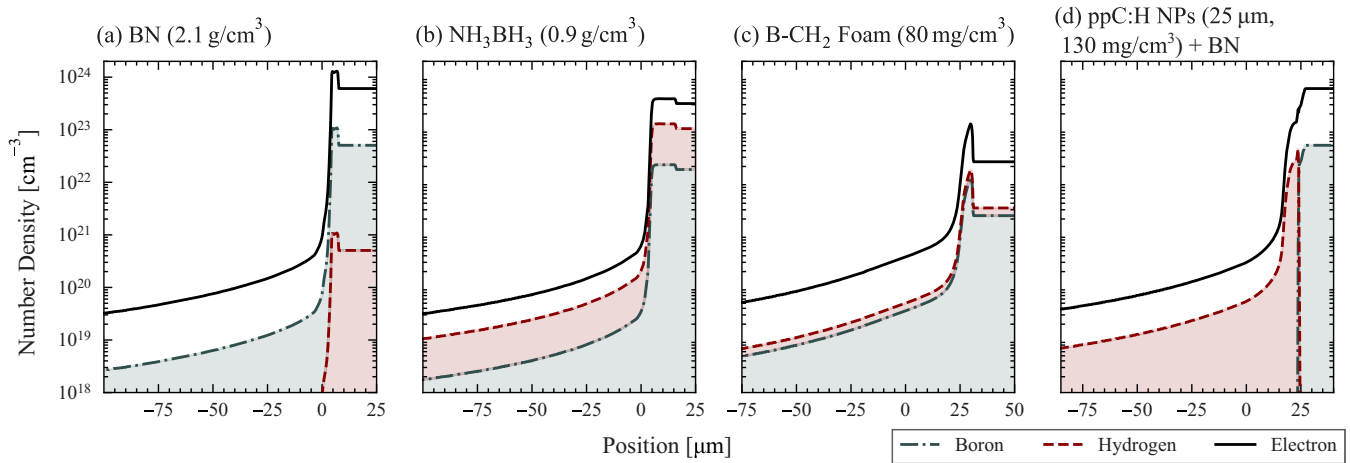


FIG. 6. The number density profile of boron, hydrogen and electrons along the target normal axis, following a 1.5 ns long pulse, incident at 20° to the target normal. The position $0\ \mu\text{m}$ corresponds to the initial surface of the target. (a) Initial target: $40\ \mu\text{m}$ BN + $50\ \text{nm}$ CH_2 , (b) ammonia-borane (NH_3BH_3) ($0.9\ \text{g cm}^{-3}$), (c) Boron- CH_2 Foam ($80\ \text{mg cm}^{-3}$, $60\ \mu\text{m}$), (d) ppC:H NPs ($130\ \text{mg cm}^{-3}$, $25\ \mu\text{m}$) on BN.

each target was modeled in 2D Cartesian geometry. The laser was incident at an angle of 20° to the target normal, with a constant peak intensity of $5 \times 10^{12}\ \text{W cm}^{-2}$. The opacity of the target materials was retrieved from the TOPS Opacity Database [48], and the equation-of-state was calculated using FEOS code [49]. All targets were modeled as homogeneous slabs, neglecting any nanostructure. It is assumed that the target would be significantly homogenized owing to the significant 1.5 ns prepulse of the laser system. The output of the radiative-hydrodynamic simulation was used to initialize the density profile in the particle-in-cell simulations.

The boron, hydrogen, and electron density profiles following irradiation by the 1.5-ns pedestal characteristic of the TARANIS laser system are presented in Fig. 6 for four different target schemes. Other species (i.e., carbon and nitrogen) are included in the hydrodynamic simulation but are omitted from the plot for clarity. Figure 6(a) presents the resulting density profiles following irradiation of a BN target. At the start of the simulation, a $10\ \text{nm}$ thick hydrocarbon contaminant layer was assumed on the surface of a BN target. Contaminant layers of this thickness are present naturally [25] and typically are thought to supply a fraction of the protons driving $p^{11}\text{B}$ fusion in the in-target configuration [24]. However, as expected [50], during the FLASH simulation, the 1.5 ns pedestal ablates the hydrocarbon contaminant layer. Therefore, it can be reasonably assumed that the hydrogen responsible for driving $p^{11}\text{B}$ fusion reactions must be caused by some contamination fraction within the target during the material synthesis. The hydrogen density presented in Fig. 6(a) is calculated assuming a hydrogen contamination fraction of 1% by number density [17,21,51]. Figure 6(b) displays the density profile of the (NH_3BH_3) target. In this case, there is a high concentration of hydrogen within the bulk of the target and throughout the preplasma owing to the high density of hydrogen in the bulk target. Because of the low density ($80\ \text{mg cm}^{-3}$) of the B- CH_2 foam, the 1.5 ns pedestal of the TARANIS laser system ablates $25\ \mu\text{m}$ of the target and generates an overdense shock that propagates through the target, compressing the target by a factor of four. As shown in Fig. 6(c), there is significant ablation of the low-density deposition by the laser pedestal. During

the experiment, the laser was focused $25\ \mu\text{m}$ beyond the target surface to compensate for this. Figure 6(d) shows the pedestal effect on a $25\ \mu\text{m}$, $130\ \text{mg cm}^{-3}$ ppC:H NPs deposition on BN. Also, in this case, because of the low density of the deposition, we observe significant target ablation. However, a $\approx 10\ \mu\text{m}$ thick hydrogen dense layer remains, which can be accelerated into the high boron density region of the target. For all targets, the target bulk has a density well beyond the hole-boring (HB) density limit defined in [52] for these experimental conditions. Therefore, any HB acceleration is confined to around the critical density surface of the preplasma generated by the pedestal.

B. Particle-In-Cell (PIC) Simulations

The interaction of the high-intensity component of the laser pulse ($8\ \text{J}$, $800\ \text{fs}$, $1053\ \text{nm}$) with the target was modeled using the WarpX [53] particle-in-cell code. The focal spot FWHM was defined as $5.1\ \mu\text{m}$, and a peak intensity of $a_0 = 4.5$. The 2D simulation box was composed of cells of size $15 \times 15\ \text{nm}$ and had minimum dimensions of $92 \times 122\ \mu\text{m}^2$. The 2D density profile for all target species (i.e., boron, hydrogen, carbon, and nitrogen if present) at the end of the hydrodynamic simulation, following a 1.5 ns pedestal, were imported into WarpX as the initial target density for the PIC simulation. The initial target was modeled as fully ionized. To reduce the computational load, the maximum electron density was capped at $160\ n_c$. This is still significantly above the hole-boring density limit for the TARANIS laser parameters [52]. At least one macroparticle per cell per n_c was used for each species. In the underdense preplasma, at least one macroparticle per cell was used per species. Multipass current smoothing and energy-conserving algorithms were used to minimize numerical heating over the three ps simulation time. Current smoothing and energy-conserving algorithms were used to minimize numerical heating over the three ps simulation time.

WarpX has implemented a pairwise nuclear collisional algorithm based on the method described in [54], which runs during the particle-in-cell algorithm using the analytical cross

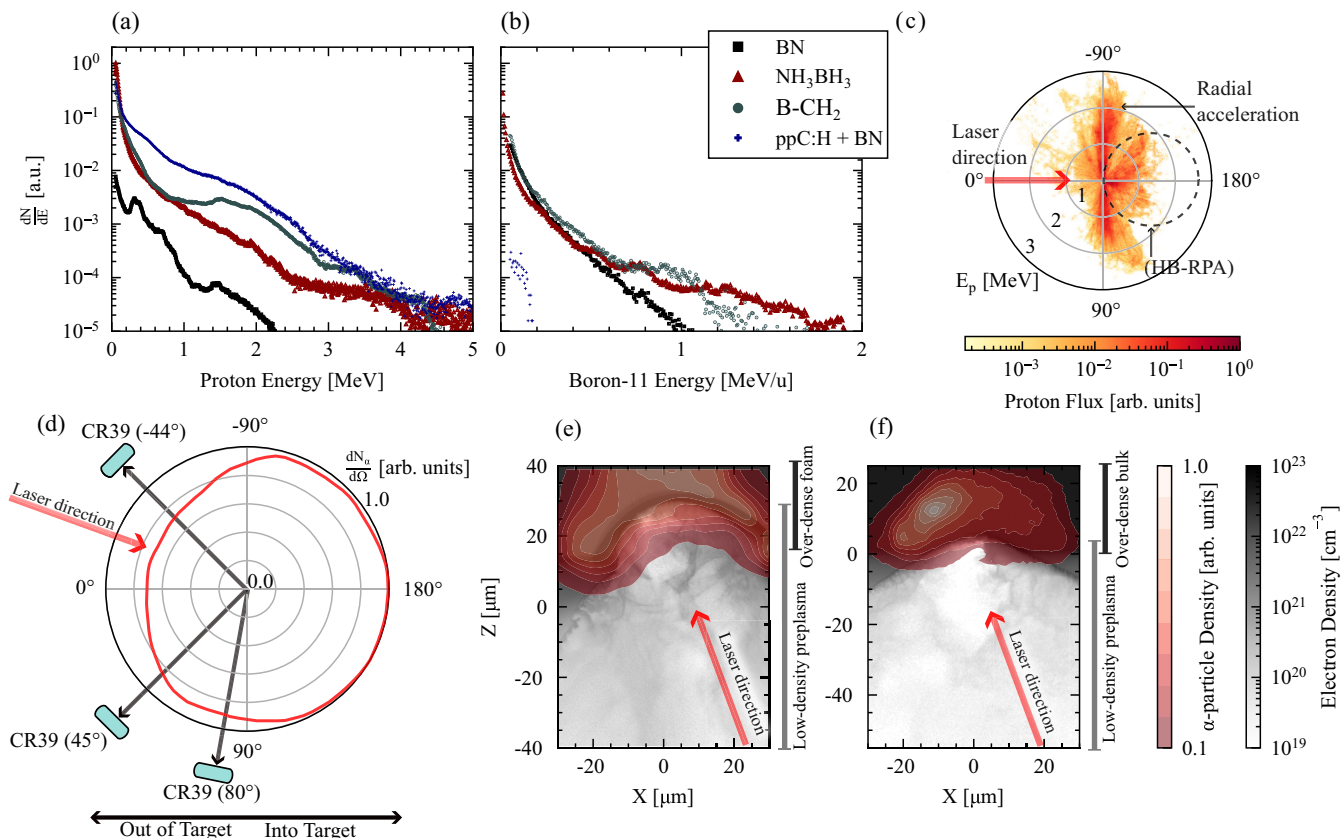


FIG. 7. Summary of results from PIC simulations. The energy spectra of (a) protons and (b) ^{11}B ions accelerated forwards into the target, 800 fs after the peak of the laser pulse. (c) Angular proton distribution 200 fs before the peak of the laser pulse, showing a high flux of protons accelerated normal to the laser axis as well as a high flux accelerated forward into the target via HB acceleration. (d) Normalized angular alpha particle flux generated in the interaction with 80 mg cm^{-3} B- CH_2 foam, 1.2 ps after the peak of the laser pulse. The positions of the CR39 detectors are annotated on the diagram. Colormap of the electron density and alpha particle density 1.8 ps after the peak of the laser pulse for the (e) 80 mg cm^{-3} B- CH_2 target and (f) (NH_3BH_3) target.

section described in [12]. This allows for the generation of alpha particles and the angular distribution and location of the proton boron fusion reactions to be retrieved from the simulation.

The results of the PIC simulations are summarized in Fig. 7. Figure 7(a) shows the energy spectrum of protons accelerated forward into the target 800 fs after the peak of the laser pulse. For all targets, it was possible to accelerate protons to energies of a few MeV, considerably above the peak in the $p^{11}\text{B}$ fusion cross section at $\approx 700\text{ keV}$, allowing the efficient generation of alpha particles.

Comparing the proton spectra presented in Fig. 7(a), a significantly higher flux of protons accelerated into the target bulk is observed when irradiating low-density depositions (i.e., 80 mg cm^{-3} B- CH_2 foam or a 130 mg cm^{-3} , $25\text{ }\mu\text{m}$ -thick ppC:H NPs deposition on a solid-density BN substrate) compared to solid density BN and (NH_3BH_3) targets. The energy coupled into protons with kinetic energy above 500 keV, was increased by approximately a factor of two when using the B- CH_2 foam target and by a factor of four when irradiation the ppC:H NPs deposition, relative to the (NH_3BH_3) target. Before the arrival of the main laser pulse, the scale length at the critical density is $(1.8 \pm 0.3)\text{ }\mu\text{m}$ for the solid (NH_3BH_3) target; however, the low-density B- CH_2 foam and ppC:H NPs

have a significantly longer scale length of $(7.0 \pm 0.6)\text{ }\mu\text{m}$ and $(4.7 \pm 0.5)\text{ }\mu\text{m}$, respectively. HB acceleration can occur until the plasma pressure of the target is greater than the radiation pressure of the laser [52]. Therefore, the longer scale length pre-plasma generated during the interaction between the laser pedestal and the low-density target depositions increases the maximum recession depth of the hole boring front. This results in a greater hole-boring velocity and a larger ion flux is accelerated into the bulk target [55,56].

Under the assumption that there is only 1% hydrogen contamination of the bulk target, the proton flux accelerated into the BN target is approximately 15 times lower than for the other targets. This highlights the need to produce targets with additional hydrogen content, particularly as the nanosecond pedestal quickly removes any naturally occurring contaminant layer. Note that a significant proton flux is still observed on the CR39, suggesting that the bulk hydrogen contamination of the BN targets could be higher than estimated. However, the hydrogen concentration has not been experimentally measured thus far.

Compared with Fig. 7(b), at energies of 1 MeV/nucleon, the flux of boron ions is over an order of magnitude lower than the proton flux. Therefore, although it is possible to accelerate boron ions with energies sufficient to drive $p^{11}\text{B}$ fusion

reactions, because of the low flux and greater stopping power ($\propto Z^2$) experienced by boron ions, their overall contribution to the fusion yield is negligible.

The polar plot presented in Fig. 7(c) displays the angular distribution of protons generated in the interaction with a B-CH₂ target, 200 fs before the peak of the laser pulse. At this early stage of the interaction, it is clear that protons are accelerated forward into the bulk target via HB acceleration, but also, a significant flux of protons are accelerated radially outwards relative to the direction of laser propagation. As observed in [57,58], electrons in an under-critical preplasma are forced radially outwards via the ponderomotive force, generating a shock that propagates outwards, accelerating protons in the radial direction. In fact, a higher flux of protons with energies above ≈ 500 keV are accelerated in the laser direction but at angles greater than 45° to the laser axis, compared to those within 45° of the laser axis. Geometrically, this results in a significant flux of protons accelerated into the boron-dense region of the target but remaining near the target surface. Alpha particles generated by these protons are, therefore, more easily able to escape the target and irradiate the CR39 detectors. This increases the number of alpha particles that can be detected experimentally. The angular distribution of protons for all four targets are presented in Appendix B.

The normalized angular distribution of alpha particles 1.2 ps after the peak of the main pulse is presented in Fig. 7(d). Because of the low energy of protons driving the p¹¹B fusion reaction, the relative flux of alpha particles into and out of the target is within $\approx 20\%$. The highest flux of alpha particles is directed at the CR39 placed at 80° to target normal.

The alpha particle density distribution 1.8 ps after the peak of the main pulse is presented in Figs. 7(e) and 7(f) for the 80 mg cm^{-3} B-CH₂ foam and the (NH₃BH₃) targets, respectively. For both targets, most of the fusion must occur within the solid target instead of the pre-plasma. This is expected as the boron density in the preplasma is several orders of magnitude lower than in the bulk target (see. Fig. 6), and the fusion reactions are primarily driven by protons accelerated forward into the target. In Figs. 7(e) and 7(f), $Z = 0 \text{ } \mu\text{m}$ corresponds to the initial target surface. In the B-CH₂ foam target, the alpha particles are generated further into the target (i.e., at greater Z) in comparison with the solid density (NH₃BH₃) target.

Experimentally, a high alpha particle flux was detected at both $\pm 45^\circ$ and 80° to target normal for the (NH₃BH₃) target, but only at $\pm 45^\circ$ for the B-CH₂ foam target. We suggest that as the fusion takes place deeper into the B-CH₂ foam target, the alpha particles ejected at 80° cannot escape the foam layer with enough energy to be detected by the CR39 detectors. In contrast, alpha particles ejected at smaller angles quickly escape the target and can be detected by the CR39.

In the case of the low-density foam target, owing to the significant ablation of the target, both protons that are accelerated forward into the target and those accelerated radially relative to the laser axis will interact with a high density of boron ions in the foam layer contributing significantly to the alpha particle flux. However, the alpha particle density distribution generated in the interaction with the solid density (NH₃BH₃) target features a clear peak corresponding to protons accelerated forward into the bulk target via HB acceleration along the laser axis.

TABLE III. Normalized alpha particle yields calculated using Eq. (2) and the energy spectrum of protons accelerated forward into the target presented in Fig. 7(a).

Target	Normalized α -particle yield
BN	1
(NH ₃ BH ₃)	7.5
ppC:H NPs (130 mg cm^{-3} , $25 \text{ } \mu\text{m}$)+BN	69
B-CH ₂ Foam (80 mg cm^{-3})	25

C. Numerical Calculations of Alpha Particle Yield

The probability that a proton with energy E_p will initiate a fusion event is given by Eq. (1), where $\sigma_{pB}(E)$ is the p¹¹B fusion cross section, n_B is the density of boron-11 ions and $\frac{dE}{dx}$ is the proton stopping power in the target,

$$P(E_p) = n_B \int_0^{E_p} \sigma_{pB}(E) \left(\frac{dE}{dx} \right)^{-1} dE. \quad (1)$$

For a proton energy distribution $\frac{dN_p}{dE_p}$, the total alpha particle yield N_α can be calculated using Eq. (2),

$$N_\alpha = 3 \int_0^{E_{\max}} \frac{dN_p}{dE_p} \cdot P(E_p) dE_p. \quad (2)$$

Using Eq. (2) we can calculate the expected alpha particle yield using the energy spectra of protons accelerated into the boron target shown in Fig. 7(a). The stopping power of protons in a cold B-CH₂, BN, and (NH₃BH₃) plasma was calculated using the erpa-dedx code [59], which is based on the ion-stopping model described in [60]. The analytical cross section described in [12] was used to calculate the fusion cross section across the energy range. The normalized alpha particle yield relative to the expected flux from a BN target is summarized in Table III. The BN target generates the lowest alpha particle yield owing to the low flux of protons accelerated into the target. The increased hydrogen content in the (NH₃BH₃) target results increases the alpha particle yield by almost an order of magnitude compared to the standard BN target. The ppC:H NPs and B-CH₂ targets produce the highest alpha particle yield because of the high flux of protons with energies above 500 keV.

Equation (1) depends on the stopping power of ions in the target. The yield from ion-driven fusion reactions strongly depends on the proton energy loss rate via ion drag [61–63]. The previous calculations assumed the stopping power of a cold target; however, in high-intensity laser-plasma interactions, the target is significantly heated through the high return current of slow, collisional electrons [64–66] and ion drag heating [61]. Thus, the electron temperature and density significantly differ from that of a cold solid target, resulting in significantly reduced proton stopping powers [17,61,67,68]. This reduction in proton energy loss has increased the number of fusion-generated alpha particles produced. This effect has been observed both in the in-target configuration [17] and the pitcher-catcher configuration when using a laser-ablated catcher [20].

Figure 8 illustrates the range of a 0.6 and 1 MeV proton propagating into an (NH₃BH₃) target with a density

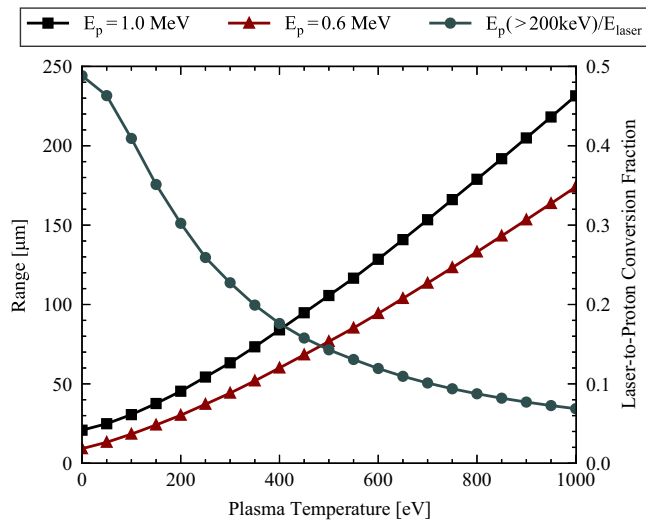


FIG. 8. A plot of the increasing range of 0.6 to 1 MeV protons in a 0.9 g cm^{-3} (NH_3BH_3) target with the target temperature and the reduction in the required laser energy converted into protons.

0.9 g cm^{-3} and a plasma temperature range 1–1000 eV. For the protons in the energy range of interest (i.e., around the 675 keV cross-section peak), there can be over an order of magnitude increase in the proton range in a hot 1 keV plasma compared to a cold target. More importantly, the range traveled while protons have an energy between 0.6 and 1 MeV (i.e., where the $p^{11}\text{B}$ fusion cross section is highest) also increases with plasma temperature. Thus, the integral in Eq. (1) greatly increases, increasing the generated alpha particle flux.

Considering the shape of the energy spectra of protons retrieved from the PIC simulation using the (NH_3BH_3) target, we can estimate the laser-to-proton energy conversion required to achieve total alpha particle yield of $10^8 \alpha/\text{sr}$, for a range of plasma temperatures. This is presented in Fig. 8. For a cold target, approximately 50% of the laser energy would need to be converted into protons with energies above 200 keV. This is far beyond what is typically expected in such laser-plasma interactions. However, as the temperature of the target is increased, the required proton conversion efficiency quickly reduces by almost a factor of seven, to 7%, at a temperature of 1 keV. While still a significant conversion efficiency, it is comparable to the values quoted in [57] under similar laser parameters in the in-target scheme. Despite the measured alpha particle yield being comparable to that described in [17] and [24] when normalized for laser energy, the required energy conversion efficiency is still greater than is expected and highlights the need for further development in modeling the transport of high current ions in the hot-dense plasma.

V. CONCLUSIONS

The high alpha particle yields recorded during this experimental campaign underscore the suitability of these novel targets for use in in-target $p^{11}\text{B}$ fusion experiments. Achieving alpha particle yields of up to $5 \times 10^7 \alpha/\text{sr}/\text{J}$, our results obtained with a ps-class laser with moderate intensity ($\approx 10^{19} \text{ W cm}^{-2}$) and energy ($\approx 10 \text{ J}$) are comparable with the highest yields obtained using very high intensity

($4 \times 10^{20} \text{ W cm}^{-2}$) femtosecond-class [24] and high energy (kJ-class) nanosecond-class [17] laser systems per J of laser energy. The alpha particle yield for each target category was calculated analytically using the proton energy spectra retrieved from the PIC simulations. Because of the high flux of protons with energies above 500 keV, the ppC:H NPs + BN and the B-CH₂ are expected to generate an alpha particle flux over an order of magnitude higher than what can be achieved with the standard BN targets. Notably, the generated alpha particle flux significantly exceeds the predictions from analytical calculations for a cold target. This substantial increase in fusion yield can partially be attributed to the reduction in ion stopping power in a hot ($\approx 1 \text{ keV}$) plasma generated in the in-target geometry.

Future experiments could utilize high-contrast laser systems and the same low-density nanostructured targets used in this campaign to enhance laser absorption further and increase the target temperature [33,69,70] for a further increase in alpha particle yield. Given the challenges of extracting alpha particle flux using CR39 detectors, future experiments could use CR39 in combination with the nuclear activation measurements of the target to unambiguously calculate the alpha particle yield [71,72].

ACKNOWLEDGMENTS

D.P.M. acknowledges the support of HB11 Energy. Research on plasma polymerized nanoparticles was supported by the Czech Science Foundation through the Grant No. GACR24-11398S. A.M. and D.O. acknowledge the financial support of the European Union Next Generation EU and Italian Ministry of University and Research as part of the PRIN 2022 program (Project ID 2022N5JBHT, ID CUP D53D23002840006). This work received support from COST Action CA21128-PROBONO “PROton BORon Nuclear fusion: from energy production to medical applications”, supported by COST (European Cooperation in Science and Technology). The authors would like to acknowledge support for this work from the EPSRC Platform Grant No. EP/P010059/1. We are grateful for the use of the computing resources from the Northern Ireland High-Performance Computing (NI-HPC) service funded by EPSRC (EP/T022175). This research used the open-source particle-in-cell code WarpX [73]. Primary WarpX contributors are with LBNL, LLNL, CEA-LIDYL, SLAC, DESY, CERN, and TAE Technologies. We acknowledge all WarpX contributors. The software used in this work was developed in part by the DOE NNSA- and DOE Office of Science-supported Flash Center for Computational Science at the University of Chicago and the University of Rochester.

DATA AVAILABILITY

The data supporting this study’s findings are available upon reasonable request from the authors.

APPENDIX A: CR39 ANALYSIS

Using conventional particle accelerators, CR39 detectors were irradiated with alpha particles at several discrete

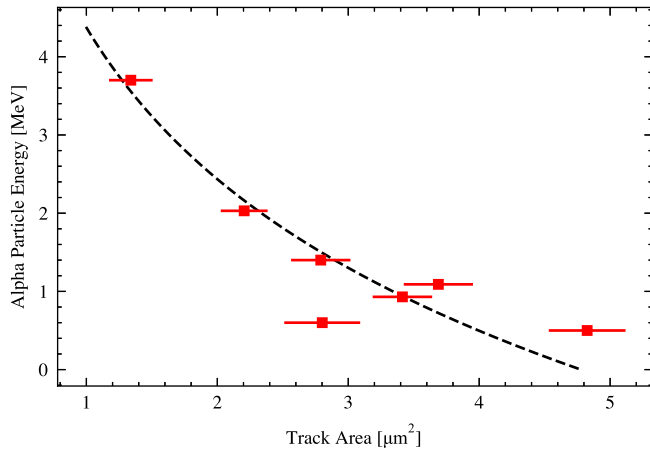


FIG. 9. A calibration of the alpha particle track size relative to the incident alpha particle energy after etching for 60 min in 6.25 M NaOH at 70 °C for energies from 0.5 MeV to 3.7 MeV.

energies ranging from 0.5 to 3.7 MeV [36,38]. The samples were etched in a 6.25 M NaOH solution at 70 °C for one hour. The damage tracks generated by the alpha particles were imaged using an optical microscope. The resulting track areas ranged from 1 to 5 μm^2 . This data is presented in Fig. 9.

While care was taken to maintain the same etching conditions for every CR39 sample (both those used in calibration and experiment), it should be noted small variations in the etching conditions (temperature and concentration of the solution), lighting when imaging the particle tracks, and the application of a binary threshold during the track identification and measurement process can result in slight variations in the particle track distribution.

As discussed in the main text and highlighted in [24,35,36], there can be significant overlap between the proton, alpha particle, and heavier ion (carbon, boron, nitrogen, etc) distributions in the particle track area distribution. The signals attributed to protons, alpha particles, and heavier ions are annotated on top of the particle track distribution in Fig. 10.

APPENDIX B: ADDITIONAL PARTICLE-IN-CELL RESULTS

Figure 11 shows the angular proton distribution 200 fs before the peak of the laser pulse of four targets: Figure 11(a) 2.1 g cm^{-3} boron nitride, Fig. 11(b) 0.9 g cm^{-3} , Fig. 11(c) 80 mg cm^{-3} B-CH₂, and Fig. 11(d) 130 mg cm^{-3} , 25 μm -thick ppC:H NPs layer on BN. The grey-shaded region denotes the angles at which protons will be accelerated into regions with a high density of boron ions. Although there will also be

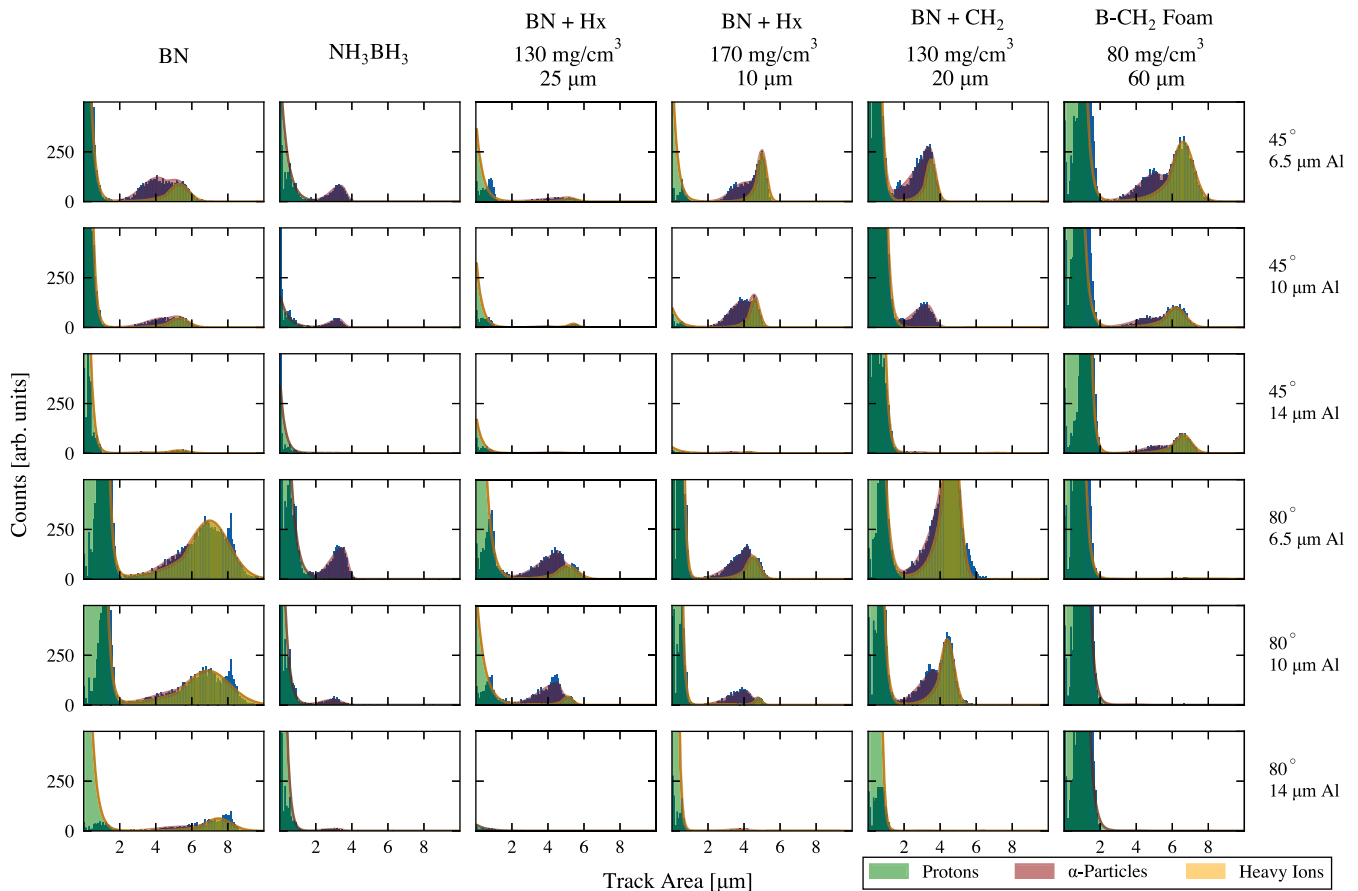


FIG. 10. Particle track area histograms extracted from CR39 detectors following etching in 6.25 M NaOH for 60 minutes. The histograms are shown for all results presented in this paper.

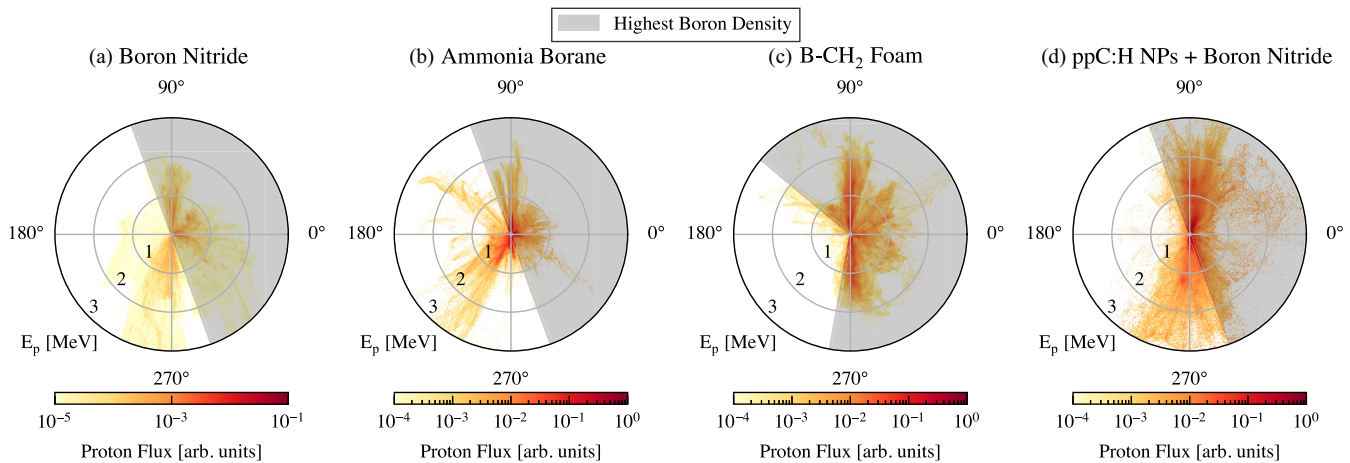


FIG. 11. The angular proton energy distribution 200 fs before the peak of the laser pulse recorded from a WarpX PIC simulation. (a) 2.1 g cm^{-3} boron nitride, (b) 0.9 g cm^{-3} , (c) 80 mg cm^{-3} B-CH₂, and (d) 130 mg cm^{-3} , $25 \text{ }\mu\text{m}$ -thick ppC:H NPs layer on BN. The proton flux from each target is normalized by the same value. 0 corresponds to the laser axis.

boron ions in the preplasma of the BN, B-CH₂, and (NH₃BH₃) targets, this is orders of magnitude less than the boron density in the main target and, therefore, is expected to have a negligible contribution to the alpha particle yield. Owing to the presence of an underdense preplasma for all targets, the angular proton distribution is comparable for all targets featuring a significant flux of protons accelerated radially relative to the laser axis as the ponderomotive force radially

displaces electrons [57,58]. It was noted that there is significant ablation of the B-CH₂ foam by the laser pedestal, resulting in the high-intensity laser-plasma interaction occurring $\approx 25 \text{ }\mu\text{m}$ below the target surface. Therefore, as shown in Fig. 11(c), compared to the other targets, both the protons accelerated in the laser direction and radially interacted with a high density of boron ions, contributing to the overall alpha particle yield.

- [1] T. A. Mehlhorn, L. Labun, B. M. Hegelich, D. Margarone, M. F. Gu, D. Batani, E. M. Campbell, S. X. Hu, and B. Ramakrishna, Path to increasing p-¹¹B reactivity via ps and ns lasers, *Laser Part. Beams* **2022**, e1 (2022).
- [2] K. Batani, Perspectives on research on laser driven proton-boron fusion and applications, *J. Instrum.* **18**, C09012 (2023).
- [3] M.-S. Liu, H.-S. Xie, Y.-M. Wang, J.-Q. Dong, K.-M. Feng, X. Gu, X.-L. Huang, X.-C. Jiang, Y.-Y. Li, Z. Li *et al.*, ENN's roadmap for proton-boron fusion based on spherical torus, *Phys. Plasmas* **31**, 062507 (2024).
- [4] W. McKenzie, D. Batani, T. A. Mehlhorn, D. Margarone, F. Belloni, E. M. Campbell, S. Woodruff, J. Kirchhoff, A. Paterson, S. Pikuz, and H. Hora, Hb11—Understanding hydrogen-boron fusion as a new clean energy source, *J. Fusion Energy* **42**, 17 (2023).
- [5] D. Moreau, Potentiality of the proton-boron fuel for controlled thermonuclear fusion, *Nucl. Fusion* **17**, 13 (1977).
- [6] W. J. Lehmann and I. Shapiro, Isotopic composition of boron and its atomic weight, *Nature (London)* **183**, 1324 (1959).
- [7] J. Bonnalet, P. Nicolai, D. Raffestin, E. D'humieres, D. Batani, V. Tikhonchuk, V. Kantarelou, L. Giuffrida, M. Tosca, G. Korn, A. Picciotto, A. Morace, Y. Abe, Y. Arikawa, S. Fujioka, Y. Fukuda, Y. Kuramitsu, H. Habara, and D. Margarone, Energetic α -particle sources produced through proton-boron reactions by high-energy high-intensity laser beams, *Phys. Rev. E* **103**, 053202 (2021).
- [8] R. Chakravarty, D. Banerjee, and S. Chakraborty, Alpha-induced production and robust radiochemical separation of ⁴³Sc as an emerging radiometal for formulation of pet radiopharmaceuticals, *Appl. Radiat. Isot.* **199**, 110921 (2023).
- [9] P. Bláha, C. Feoli, S. Agosteo, M. Calvaruso, F. P. Cammarata, R. Catalano, M. Ciocca, G. A. P. Cirrone, V. Conte, G. Cuttone *et al.*, The proton-boron reaction increases the radiobiological effectiveness of clinical low- and high-energy proton beams: Novel experimental evidence and perspectives, *Front. Oncol.* **11**, 682647 (2021).
- [10] G. A. Cirrone, L. Manti, D. Margarone, G. Petringa, L. Giuffrida, A. Minopoli, A. Picciotto, G. Russo, F. Cammarata, P. Pisciotto *et al.*, First experimental proof of proton boron capture therapy (PBCT) to enhance protontherapy effectiveness, *Sci. Rep.* **8**, 1141 (2018).
- [11] M. H. Sikora and H. R. Weller, A new evaluation of the ¹¹B(p, α) α reaction rates, *J. Fusion Energy* **35**, 538 (2016).
- [12] A. Tentori and F. Belloni, Revisiting p-¹¹B fusion cross section and reactivity, and their analytic approximations, *Nucl. Fusion* **63**, 086001 (2023).
- [13] W. M. Nevins and R. Swain, The thermonuclear fusion rate coefficient for p-¹¹B reactions, *Nucl. Fusion* **40**, 865 (2000).
- [14] R. A. Snavelly, M. H. Key, S. P. Hatchett, T. E. Cowan, M. Roth, T. W. Phillips, M. A. Stoyer, E. A. Henry, T. C. Sangster, M. S. Singh, S. C. Wilks, A. Mackinnon, A. Offenberger, D. M. Pennington, K. Yasuike, A. B. Langdon, B. F. Lasinski, J. Johnson, M. D. Perry, and E. M. Campbell, Intense high-energy proton beams from petawatt-laser irradiation of solids, *Phys. Rev. Lett.* **85**, 2945 (2000).

- [15] T. Schlegel, N. Naumova, V. T. Tikhonchuk, C. Labaune, I. V. Sokolov, and G. Mourou, Relativistic laser piston model: Ponderomotive ion acceleration in dense plasmas using ultraintense laser pulses, *Phys. Plasmas* **16**, 083103 (2009).
- [16] A. Henig, D. Kiefer, M. Geissler, S. G. Rykovanov, R. Ramis, R. Hörlein, J. Osterhoff, Z. Major, L. Veisz, S. Karsch, F. Krausz, D. Habs, and J. Schreiber, Laser-driven shock acceleration of ion beams from spherical mass-limited targets, *Phys. Rev. Lett.* **102**, 095002 (2009).
- [17] L. Giuffrida, F. Belloni, D. Margarone, G. Petringa, G. Milluzzo, V. Scuderi, A. Velyhan, M. Rosinski, A. Picciotto, M. Kucharik, J. Dostal, R. Dudzak, J. Krasa, V. Istoksaia, R. Catalano, S. Tudisco, C. Verona, K. Jungwirth, P. Bellutti, G. Korn *et al.*, High-current stream of energetic α particles from laser-driven proton-boron fusion, *Phys. Rev. E* **101**, 013204 (2020).
- [18] V. Istoksaia, M. Tosca, L. Giuffrida, J. Psikal, F. Grepl, V. Kantarelou, S. Stancek, S. D. Siena, A. Hadjikyriacou, A. McIlvenny *et al.*, A multi-MeV alpha particle source via proton-boron fusion driven by a 10-GW tabletop laser, *Commun. Phys.* **6**, 27 (2023).
- [19] V. S. Belyaev, A. P. Matafonov, S. N. Andreev, V. P. Tarakanov, V. P. Krainov, V. S. Lisitsa, A. Y. Kedrov, B. V. Zagreev, A. S. Rusetskii, N. G. Borisenko *et al.*, Investigation of the yield of the nuclear reaction $^{11}\text{B}(p, 3\alpha)$ initiated by powerful picosecond laser radiation, *Phys. At. Nucl.* **85**, 31 (2022).
- [20] C. Labaune, C. Baccou, S. Depierreux, C. Goyon, G. Loisel, V. Yahia, and J. Rafelski, Fusion reactions initiated by laser-accelerated particle beams in a laser-produced plasma, *Nat. Commun.* **4**, 2506 (2013).
- [21] D. Margarone, J. Bonvalet, L. Giuffrida, A. Morace, V. Kantarelou, M. Tosca, D. Raffestin, P. Nicolai, A. Picciotto, Y. Abe *et al.*, In-target proton-boron nuclear fusion using a PW-class laser, *Appl. Sci.* **12**, 1444 (2022).
- [22] A. Picciotto, D. Margarone, A. Velyhan, P. Bellutti, J. Krasa, A. Szydłowski, G. Bertuccio, Y. Shi, A. Mangione, J. Prokupek, A. Malinowska, E. Krousky, J. Ullschmied, L. Laska, M. Kucharik, and G. Korn, Boron-proton nuclear-fusion enhancement induced in boron-doped silicon targets by low-contrast pulsed Laser, *Phys. Rev. X* **4**, 031030 (2014).
- [23] V. S. Belyaev, A. P. Matafonov, V. I. Vinogradov, V. P. Krainov, V. S. Lisitsa, A. S. Roussetski, G. N. Ignatyev, and V. P. Adrianov, Observation of neutronless fusion reactions in picosecond laser plasmas, *Phys. Rev. E* **72**, 026406 (2005).
- [24] M. S. Schollmeier, J. J. Bekx, J. Hartmann, E. Schork, M. Speicher, A. F. Brodersen, A. Fazzini, P. Fischer, E. Gaul, B. Gonzalez-Izquierdo *et al.*, Differentiating multi-MeV, multi-ion spectra with CR-39 solid-state nuclear track detectors, *Sci. Rep.* **13**, 18155 (2023).
- [25] Z. Léczy, J. Budai, A. Andreev, and S. Ter-Avetisyan, Thickness of natural contaminant layers on metal surfaces and its effects on laser-driven ion acceleration, *Phys. Plasmas* **27**, 013105 (2020).
- [26] T. Dzelzainis, G. Nersisyan, D. Riley, L. Romagnani, H. Ahmed, A. Bigongiari, M. Borghesi, D. Doria, B. Dromey, M. Makita *et al.*, The TARANIS laser: A multi-Terawatt system for laser-plasma investigations, *Laser Part. Beams* **28**, 451 (2010).
- [27] M. Tosca, D. Molloy, A. McNamee, P. Pleskunov, M. Protsak, K. Biliak, D. Nikitin, J. Kousal, Z. Krtouš, L. Hanyková *et al.*, Plasma polymers as targets for laser-driven proton-boron fusion, *Front. Phys.* **11**, 1227140 (2023).
- [28] P. Solař, O. Polonskyi, A. Choukourov, A. Artemenko, J. Hanuš, H. Biederman, and D. Slavínská, Nanostructured thin films prepared from cluster beams, *Surf. Coat. Technol.* **205**, S42 (2011).
- [29] A. Choukourov, P. Pleskunov, D. Nikitin, V. Titov, A. Shelemin, M. Vaidulych, A. Kuzminova, P. Solař, J. Hanuš, J. Kousal *et al.*, Advances and challenges in the field of plasma polymer nanoparticles, *Beilstein J. Nanotechnol.* **8**, 2002 (2017).
- [30] A. Picciotto, M. Valt, D. P. Molloy, A. Gaiardo, A. Milani, V. Kantarelou, L. Giuffrida, G. Nersisyan, A. McNamee, J. P. Kennedy *et al.*, Ammonia borane-based targets for new developments in laser-driven proton boron fusion, *Appl. Surf. Sci.* **672**, 160797 (2024).
- [31] F. Belloni, On a fusion chain reaction via suprathermal ions in high-density $\text{H-}^{11}\text{B}$ plasma, *Plasma Phys. Controlled Fusion* **63**, 055020 (2021).
- [32] F. Belloni, Multiplication processes in high-density $\text{H-}^{11}\text{B}$ fusion fuel, *Laser Part. Beams* **2022**, e11 (2022).
- [33] M. Passoni, F. M. Arioli, L. Cialfi, D. Dellasega, L. Fedeli, A. Formenti, A. C. Giovannelli, A. Maffini, F. Mirani, A. Pazzaglia *et al.*, Advanced laser-driven ion sources and their applications in materials and nuclear science, *Plasma Phys. Controlled Fusion* **62**, 014022 (2020).
- [34] D. Orecchia, A. Maffini, M. Zavelani-Rossi, and M. Passoni, Versatile synthesis of nanofoams through femtosecond pulsed laser deposition, *Small Struct.* **5**, 2300560 (2024).
- [35] C. Baccou, V. Yahia, S. Depierreux, C. Neuville, C. Goyon, F. Consoli, R. De Angelis, J. E. Ducret, G. Boutoux, J. Rafelski, and C. Labaune, CR-39 track detector calibration for H, He, and C ions from 0.1–0.5 MeV up to 5 MeV for laser-induced nuclear fusion product identification, *Rev. Sci. Instrum.* **86**, 083307 (2015).
- [36] V. Kantarelou, A. Velyhan, P. Tchórz, M. Rosiński, G. Petringa, G. A. P. Cirrone, V. Istoksaia, J. Krása, M. Krús, A. Picciotto *et al.*, A methodology for the discrimination of alpha particles from other ions in laser-driven proton-boron reactions using CR-39 detectors coupled in a Thomson parabola spectrometer, *Laser Part. Beams* **2023**, e10 (2023).
- [37] J. F. Ziegler, M. Ziegler, and J. Biersack, SRIM—The stopping and range of ions in matter (2010), *Nucl. Instrum. Methods Phys. Res. Sect. B* **268**, 1818 (2010).
- [38] G. Petringa, V. Kantarelou, R. Catalano, G. Cantone, O. Giampiccolo, G. Messina, G. Angemi, S. Arjmand, E. Caruso, G. Cuttone *et al.*, CR-39 track detector calibration with H and He beams for applications in the $\text{p-}^{11}\text{B}$ fusion reaction, *J. Instrum.* **19**, C04044 (2024).
- [39] M. C. Spraker, M. W. Ahmed, M. A. Blackston, N. Brown, R. H. France, S. S. Henshaw, B. A. Perdue, R. M. Prior, P. N. Seo, S. Stave, and H. R. Weller, The $^{11}\text{B}(p, \alpha)^8\text{Be} \rightarrow \alpha + \alpha$ and the $^{11}\text{B}(\alpha, \alpha)^{11}\text{B}$ reactions at energies below 5.4 MeV, *J. Fusion Energy* **31**, 357 (2012).
- [40] M. N. Quinn, X. H. Yuan, X. X. Lin, D. C. Carroll, O. Tresca, R. J. Gray, M. Coury, C. Li, Y. T. Li, C. M. Brenner *et al.*, Refluxing of fast electrons in solid targets irradiated by intense, picosecond laser pulses, *Plasma Phys. Controlled Fusion* **53**, 025007 (2011).

- [41] T. Ceccotti, A. Lévy, H. Popescu, F. Réau, P. D'Oliveira, P. Monot, J. P. Geindre, E. Lefebvre, and P. Martin, Proton acceleration with high-intensity ultrahigh-contrast laser pulses, *Phys. Rev. Lett.* **99**, 185002 (2007).
- [42] C. Baccou, S. Depierreux, V. Yahia, C. Neuville, C. Goyon, R. D. Angelis, F. Consoli, J. Ducret, G. Boutoux, J. Rafelski, and C. Labaune, New scheme to produce aneutronic fusion reactions by laser-accelerated ions, *Laser Part. Beams* **33**, 117 (2015).
- [43] M. Tayyab, S. Bagchi, A. Moorti, and J. A. Chakera, Experimental investigation on nuclear reactions using a laser-accelerated proton and deuteron beam, *Plasma Phys. Controlled Fusion* **61**, 115007 (2019).
- [44] L. Giuffrida, K. Svensson, J. Psikal, D. Margarone, P. Lutoslawski, V. Scuderi, G. Milluzzo, J. Kaufman, T. Wiste, M. Dalui *et al.*, Nano and micro structured targets to modulate the spatial profile of laser driven proton beams, *J. Instrum.* **12**, C03040 (2017).
- [45] B. Fryxell, K. Olson, P. Ricker, F. X. Timmes, M. Zingale, D. Q. Lamb, P. Macneice, R. Rosner, J. W. Truran, and H. Tufo, FLASH: An adaptive mesh hydrodynamics code for modeling astrophysical thermonuclear flashes, *Astrophys. J. Suppl. Ser.* **131**, 273 (2000).
- [46] FLASH, Flash website (2022), <https://flash.rochester.edu/site/index.shtml>.
- [47] C. Orban, M. Fatenejad, S. Chawla, S. C. Wilks, and D. Q. Lamb, A radiation-hydrodynamics code comparison for laser-produced plasmas: Flash versus hydra and the results of validation experiments, [arXiv:1306.1584](https://arxiv.org/abs/1306.1584).
- [48] Los Alamos National Security, LLC, TOPS opacities (2024).
- [49] S. Faik, A. Tauschwitz, and I. Iosilevskiy, The equation of state package FEOS for high energy density matter, *Comput. Phys. Commun.* **227**, 117 (2018).
- [50] J. C. Fernandez, B. Hegelich, J. Cobble, K. Flippo, S. Letzring, R. P. Johnson, D. Gautier, T. Shimada, G. Kyrala, Y. Wang, C. Wetzeland, and J. Schreiber, Laser-ablation treatment of short-pulse laser targets: Toward an experimental program on energetic-ion interactions with dense plasmas, *Laser Part. Beams* **23**, 267 (2005).
- [51] D. Margarone, A. Morace, J. Bonvalet, Y. Abe, V. Kantarelou, D. Raffestin, L. Giuffrida, P. Nicolai, M. Tosca, A. Picciotto *et al.*, Generation of α -particle beams with a multi-kJ, peta-Watt class laser system, *Front. Phys.* **8**, 343 (2020).
- [52] N. Iwata, S. Kojima, Y. Sentoku, M. Hata, and K. Mima, Plasma density limits for hole boring by intense laser pulses, *Nat. Commun.* **9**, 623 (2018).
- [53] WarpX, WarpX (2022), <https://github.com/ECP-WarpX/WarpX>.
- [54] D. P. Higginson, A. Link, and A. Schmidt, A pairwise nuclear fusion algorithm for weighted particle-in-cell plasma simulations, *J. Comput. Phys.* **388**, 439 (2019).
- [55] J. Hornung, Y. Zobus, S. Roeder, A. Kleinschmidt, D. Bertini, M. Zepf, and V. Bagnoud, Time-resolved study of holeboring in realistic experimental conditions, *Nat. Commun.* **12**, 6999 (2021).
- [56] N. Izumi, Y. Sentoku, H. Habara, K. Takahashi, F. Ohtani, T. Sonomoto, R. Kodama, T. Norimatsu, H. Fujita, Y. Kitagawa, K. Mima, K. A. Tanaka, and T. Yamanaka, Observation of neutron spectrum produced by fast deuterons via ultraintense laser plasma interactions, *Phys. Rev. E* **65**, 036413 (2002).
- [57] H. Habara, K. L. Lancaster, S. Karsch, C. D. Murphy, P. A. Norreys, R. G. Evans, M. Borghesi, L. Romagnani, M. Zepf, T. Norimatsu, Y. Toyama, R. Kodama, J. A. King, R. Snavely, K. Akli, B. Zhang, R. Freeman, S. Hatchett, A. J. MacKinnon, P. Patel *et al.*, Ion acceleration from the shock front induced by hole boring in ultraintense laser-plasma interactions, *Phys. Rev. E* **70**, 046414 (2004).
- [58] P. Kordell, C. Zulick, A. E. Hussein, A. V. Arefiev, T. Batson, J. Cobble, V. Glebov, D. Haberberger, C. Stoeckl, P. M. Nilson, K. Krushelnick, and L. Willingale, Quasi-monoenergetic ion acceleration and neutron generation from laser-driven transverse collisionless shocks, *Phys. Plasmas* **31**, 103110 (2024).
- [59] I. E. Golovkin, Development of Ion Stopping Models for HED Plasmas Using Unified Self-Consistent Field Models and Self-Consistent Electron Distributions, Technical Report No. US2309497, Prism Computational Sciences, Madison, WI, USA, 2022.
- [60] P. Wang, T. M. Mehlhorn, and J. J. MacFarlane, A unified self-consistent model for calculating ion stopping power in ICF plasma, *Phys. Plasmas* **5**, 2977 (1998).
- [61] A. P. L. Robinson, Intense laser-generated ion beams propagating in plasmas, *Plasma Phys. Controlled Fusion* **64**, 105014 (2022).
- [62] A. P. L. Robinson, Intense laser-generated ion beams in plasmas: The rapid heating regime, *Plasma Phys. Controlled Fusion* **65**, 055004 (2023).
- [63] A. P. L. Robinson, Reduction of fast ion drag in the presence of 'hollow' non-Maxwellian electron distributions, *Plasma Phys. Controlled Fusion* **66**, 035017 (2024).
- [64] A. R. Bell, J. R. Davies, S. Guerin, and H. Ruhl, Fast-electron transport in high-intensity short-pulse laser - solid experiments, *Plasma Phys. Controlled Fusion* **39**, 653 (1997).
- [65] R. H. H. Scott, F. Perez, J. J. Santos, C. P. Ridgers, J. R. Davies, K. L. Lancaster, S. D. Baton, P. Nicolai, R. M. G. M. Trines, A. R. Bell *et al.*, A study of fast electron energy transport in relativistically intense laser-plasma interactions with large density scalelengths, *Phys. Plasmas* **19**, 053104 (2012).
- [66] A. Robinson, D. Strozzi, J. Davies, L. Gremillet, J. Honrubia, T. Johzaki, R. Kingham, M. Sherlock, and A. Solodov, Theory of fast electron transport for fast ignition, *Nucl. Fusion* **54**, 054003 (2014).
- [67] X. Ning, T. Liang, D. Wu, S. Liu, Y. Liu, T. Hu, Z. Sheng, J. Ren, B. Jiang, Y. Zhao, D. H. H. Hoffmann, X. He, and D. Batani, Laser-driven proton-boron fusions: Influences of the boron state, *Laser Part. Beams* **2022**, e8 (2022).
- [68] A. B. Zylstra, J. A. Frenje, P. E. Grabowski, C. K. Li, G. W. Collins, P. Fitzsimmons, S. Glenzer, F. Graziani, S. B. Hansen, S. X. Hu, M. G. Johnson, P. Keiter, H. Reynolds, J. R. Rygg, F. H. Séguin, and R. D. Petrasso, Measurement of charged-particle stopping in warm dense plasma, *Phys. Rev. Lett.* **114**, 215002 (2015).
- [69] D. Margarone, O. Klimo, I. J. Kim, J. Prokúpek, J. Limpouch, T. M. Jeong, T. Mocek, J. Pšikal, H. T. Kim, J. Proška, K. H. Nam, L. Štolcová, I. W. Choi, S. K. Lee, J. H. Sung, T. J. Yu, and G. Korn, Laser-driven proton acceleration enhancement by nanostructured foils, *Phys. Rev. Lett.* **109**, 234801 (2012).

- [70] M. Tosca, A. Morace, M. Schollmeier, S. Steinke, V. Shirvanyan, Y. Arikawa, L. Giuffrida, D. Margarone, P. Pleskunov, A. Choukourov, R. R. Whitney, L. R. Scammell, and G. Korn, Enhanced laser absorption and ion acceleration by boron nitride nanotube targets and high-energy PW laser pulses, *Phys. Rev. Res.* **6**, 023326 (2024).
- [71] M. R. D. Rodrigues, A. Bonasera, M. Scisciò, J. A. Pérez-Hernández, M. Ehret, F. Filippi, P. L. Andreoli, M. Huault, H. Larreur, D. Singappuli *et al.*, Radioisotope production using lasers: From basic science to applications, *Matter Radiat. Extremes* **9**, 037203 (2024).
- [72] B. M. Hegelich, L. Labun, O. Z. Labun, T. A. Mehlhorn, and D. Batani, Photon and neutron production as *in situ* diagnostics of proton-boron fusion, *Laser Part. Beams* **2023**, e7 (2023).
- [73] <https://github.com/ECP-WarpX/WarpX>.